

Multi-wavelength ALMA Imaging of HD 34282: Dust-trapping Signatures of a Vortex Candidate

XIAOYI MA (马潇依),^{1,2} FANGYUAN YU (俞方远),³ RUOBING DONG (董若冰),¹ KIYOAKI DOI,⁴ AKIMASA KATAOKA,⁵ HAUYU BAOBAB LIU,^{6,7} FENG LONG (龙凤),¹ TAKAHIRO UEDA,⁵ HUOJUN LI (李火骏),² NIENKE VAN DER MAREL,⁸ AND ÁGNES KÓSPÁL^{9,10}

¹*Kaoli Institute for Astronomy and Astrophysics, Peking University, Beijing 100871, China*

²*Department of Astronomy, School of Physics, Peking University, Beijing 100871, China*

³*Department of Astrophysical Sciences, Princeton University, 4 Ivy Lane, Princeton, NJ 08544, USA*

⁴*Max-Planck-Institut für Astronomie, Königstuhl 17, 69117 Heidelberg, Germany*

⁵*National Astronomical Observatory of Japan, 2-21-1 Osawa, Mitaka, Tokyo 181-8588, Japan*

⁶*Department of Physics, National Sun Yat-Sen University, No. 70, Lien-Hai Road, Kaohsiung City 80424, Taiwan, R.O.C.*

⁷*Center of Astronomy and Gravitation, National Taiwan Normal University, Taipei 116, Taiwan*

⁸*Leiden Observatory, Leiden University, P.O. Box 9513, 2300 RA Leiden, The Netherlands*

⁹*Konkoly Observatory, HUN-REN Research Centre for Astronomy and Earth Sciences, MTA Centre of Excellence, Konkoly-Thege Miklós út 15-17, 1121 Budapest, Hungary*

¹⁰*Max-Planck-Institut für Astronomie, Königstuhl 17, 69117 Heidelberg, Germany*

ABSTRACT

Azimuthal arcs in millimeter continuum emission from protoplanetary disks are often attributed to dust-trapping vortices, but definitive observational confirmation of vortices remains lacking. We present sub-0.1'' resolution ALMA continuum observations of the HD 34282 disk at 0.9, 1.3, 2.1, and 3.1 mm. These observations resolve a bright azimuthal arc superposed on a compact double-gap, triple-ring morphology, most clearly at shorter wavelengths, and enable us to probe the physical origin of the arc. It exhibits a lower spectral index than the surrounding rings, consistent with enhanced grain growth and/or higher dust surface density of a dust-trapping vortex. Its azimuthal width decreases with increasing wavelength, consistent with tighter confinement of larger grains, or lower optical depths at longer wavelengths. These observations probe dust with Stokes numbers $St \lesssim 0.03$. Vortex models predict negligible peak shifts in this regime, consistent with the 1.3–3.1 mm data. At 0.9 mm, however, the arc peak is offset by $\sim 15^\circ \pm 4^\circ$ in the direction of disk rotation relative to longer wavelengths, and the near-side ring emission is locally dimmer compared to the far-side, likely reflecting optical-depth or temperature effects. These observations are consistent with azimuthal dust trapping, potentially associated with a vortex-induced pressure maximum.

1. INTRODUCTION

High-resolution observations of protoplanetary disks reveal that substructures are ubiquitous (e.g., Andrews et al. 2018; Long et al. 2018). Many systems exhibit axisymmetric rings and gaps in disks, while a subset shows striking azimuthal arcs in the millimeter continuum (e.g., van der Marel et al. 2021; Curone et al. 2025). Millimeter continuum arcs are typically observed at radii of tens to hundreds of au and span a finite azimuthal extent, ranging from 20° to 170° , often well shorter than

a full ring (e.g., van der Marel et al. 2013; Casassus et al. 2015; van der Marel et al. 2016; Dong et al. 2018b; van der Marel et al. 2021; Curone et al. 2025). When resolved, they are radially compact and are often embedded within ring structures, suggesting localized dust enhancements (van der Marel et al. 2015). A range of physical mechanisms have been proposed to explain azimuthal arcs, and their origins are not uniquely constrained.

A leading explanation for the observed arcs is azimuthal dust trapping, potentially associated with long-lived anticyclonic vortices, arising from the Rossby-wave instability (RWI) at sharp vortensity gradients in low-turbulence disks (Lovelace & Hohlfield 1978; Lovelace et al. 1999; Li et al. 2000; Ono et al. 2018), such as at

planet-carved gap edges (Zhu et al. 2014; Zhu & Stone 2014; Cimerman & Rafikov 2023) or viscosity transitions (Regály et al. 2012; Flock et al. 2015). These vortices act as local high-pressure maxima that trap dust both azimuthally and radially (Lyra et al. 2008; Lin 2012; Baruteau & Zhu 2016). By concentrating dust, they increase local dust-to-gas ratio, which may enable the streaming instability (Stammler et al. 2019). This accelerates grain growth and coagulation within the vortex (Birnstiel et al. 2013; Fu et al. 2014), making vortices plausible planetesimal birth sites (Meheut et al. 2012). Moreover, vortices can also sculpt rings and gaps by launching density waves (Paardekooper et al. 2010), further trapping dust, which may facilitate later stages of planet formation (Ma et al. 2025). Identifying these features in disks is therefore crucial for linking observed substructures to the mechanisms that govern planet formation.

In addition to continuum observations, vortices may also be revealed by scattered-light imaging that traces micrometer-sized grains on disk surfaces. Simulations predict that vortices appear as bright single-arm spirals and cast shadows (Marr & Dong 2022) in scattered-light images for moderately inclined disks. Among disks with mm-continuum arcs, only a few have high-sensitivity, high-resolution scattered light data, such as HD 34282 (van der Plas et al. 2017; de Boer et al. 2021; Curone et al. 2025), HD 142527 (Casassus et al. 2015; Marino et al. 2015), HD 135344B (Stolker et al. 2016; van der Marel et al. 2016), V1247 Ori (Kraus et al. 2017), MWC 758 (Boehler et al. 2018; Dong et al. 2018b), and AB Aurigae (Tang et al. 2017; Boccaletti et al. 2020). Only some of these systems show spiral-like scattered-light features that spatially coincide with the mm arc, together with an outer-disk shadow (e.g., HD 34282; Marr & Dong 2022).

However, definitive evidence of vortices in gas motion is still lacking, and alternative explanations to observed arcs have been proposed, such as pile-ups of material at apocenter in eccentric disks (Ataiee et al. 2013; Ragusa et al. 2017, 2020). A vortex should exhibit distinct kinematic signatures in gas velocity fields compared to the eccentric disk scenario. To date, such signatures remain elusive. Non-Keplerian velocity perturbations consistent with pressure maxima have been reported in HD 142527 (Boehler et al. 2018; Yen & Gu 2020), but they are not uniquely attributable to vortical motion (Ragusa et al. 2017; Boehler et al. 2021). More recent ALMA gas observations of disks with mm continuum arcs also did not reveal unambiguous vortex kinematic signatures (Wölfer et al. 2025; Stadler et al. 2026).

In millimeter dust emission, multi-wavelength observations provide a powerful and accessible diagnostic of azimuthal dust trapping in vortices. Arcs are expected to narrow at longer wavelengths because larger grains are more efficiently trapped (Birnstiel et al. 2013), as observed in IRS 48 (van der Marel et al. 2015), MWC 758 (Marino et al. 2015), HD 142527 (Casassus et al. 2015), HD 135344B (Cazzoletti et al. 2018), and PDS 70 (Doi et al. 2024). However, this trend alone supports dust trapping and does not uniquely establish a vortex origin. Analytic steady-state vortex prescriptions (Lyra & Lin 2013) link continuum morphology to vortex parameters and enable forward modeling under specific dust assumptions. For example, the aspect ratio and wavelength dependence of the arc azimuthal width in MWC 758 have been successfully modeled using these vortex prescriptions (Casassus et al. 2019). Hydrodynamic simulations also predict a wavelength-dependent azimuthal shift of the dust trapping location in vortices (Baruteau & Zhu 2016). In HD 135344B, multi-wavelength ALMA data show a shift, but in a direction inconsistent with theoretical expectations (Cazzoletti et al. 2018).

We present new high-resolution, high-sensitivity ALMA continuum observations of the HD 34282 disk at 3.1, 2.1, and 0.9 mm, together with archival 1.3 mm data. These data allow us to test the wavelength-dependent emission properties within the azimuthal arc and assess whether it is consistent with dust trapping. HD 34282 is a Herbig Ae star located at a distance of 309 ± 2 pc, with a stellar mass of approximately $1.5 M_{\odot}$, age of ~ 6.4 Myr, a luminosity of $\sim 13.6 L_{\odot}$ (Gaia Collaboration et al. 2023). It hosts a transition disk with inclination $i \sim 60^{\circ}$ with a cavity of ~ 80 au in millimeter dust observations (van der Plas et al. 2017). The disk exhibits a scattered-light spiral co-spatial with the mm-bright arc and an outer-disk shadow, making the structure a strong vortex candidate (de Boer et al. 2021; Marr & Dong 2022). Existing ^{12}CO and ^{13}CO molecular line observations did not show distinctive kinematic signature of the vortex in HD 34282 likely due to insufficient sensitivity and resolution (Law et al. 2023; Wölfer et al. 2025).

The paper is organized as follows. §2 describes the observations and data reduction processes. §3 presents the disk morphology and visibility modeling. §4 tests theoretical predictions of dust trapping against the observations. §5 discusses additional features at 0.9 mm beyond the rings and arc. Finally, §6 summarizes our main findings.

2. OBSERVATIONS & DATA REDUCTION

In this section, we summarize the observations (§2.1) and data reduction (§2.2). Table 1 lists the key dataset and image characteristics.

2.1. Observations

We analyze HD 34282 using new ALMA continuum observations at 3.1, 2.1, and 0.9 mm (Bands 3, 4, and 7) together with archival 1.3 mm data (Band 6) (Francis & van der Marel 2020) to characterize the disk asymmetry at high angular resolution and sensitivity.

Band 3 observations were conducted in ALMA Cycle 10 between May and June 2023 as part of program 2022.1.00315.S (PI: R. Dong). The correlator was configured with four spectral windows in dual polarization and time division mode (TDM). Spectral windows are centered at 90.521, 92.416, 102.521, and 104.479 GHz with 128 channels each 15.625 MHz in width, spanning a total bandwidth of 2 GHz in each spectral window. The observations were carried out in both extended (long-baseline; LB) and compact (short-baseline; SB) configurations to achieve high spatial resolution while preserving large maximum recoverable scales for accurate total flux recovery. The SB observations used C-6 configuration of 42 antennas with baselines from 15.3 m to 2.5 km for a total on-source integration time of ~ 49 min. The LB observations comprised four execution blocks with 47, 49, 47, and 48 antennas using C-9 configuration, covering baselines from 226.5 m to 15.2 km, with a total on-source integration time of ~ 142 min.

Band 4 observations were conducted in ALMA Cycle 10 between May and July 2023 as a part of program 2022.1.00315.S. The correlator was configured in dual polarization and TDM mode with the spectral windows centered at 138.021, 139.916, 150.021, and 151.979 GHz. The SB observations used C-6 configuration of 40 antennas with baselines from 15.2 m to 2.5 km for a total on-source integration time of ~ 34 min. The LB observations comprised two execution blocks with 43 and 38 antennas using C-9 configuration, covering baselines from 113.3 m to 9.7 km, with a total on-source integration time of ~ 82 min.

Band 6 data comprise archival observations, including SB executions from Cycle 3 (program 2015.1.00192.S, PI: G. van der Plas) and LB executions from Cycle 5 (program 2017.1.02578.S, PI: J. de Boer). We used the processed dataset in which the SB and LB executions were concatenated, as presented by Francis & van der Marel (2020), which has SNR ~ 55 and a synthesized beam of $0.056 \times 0.051''$. The observational setup and

calibration procedures are described in detail in Francis & van der Marel (2020).

The Band 7 data included SB and LB observations executed from different programs. The LB observations at Band 7 were conducted on September 24, 2023 as part of program 2022.1.00315.S, with C-7 configuration of 41 and 45 antennas in two execution blocks covering baselines from 66.8 m to 5.8 km for a total on-source integration time of ~ 74 min. The correlator was configured in TDM mode with spectral windows centered at 336.512, 338.416, 348.521, and 350.479 GHz. The SB observations were conducted in ALMA Cycle 11 on December 23, 2023 as a part of 2023.1.00108.S (PI: X. Ma) using 45 antennas with baselines from 15.1 m to 1.2 km using C-4 configuration for a total on-source integration time of ~ 20 min. The correlator has the same spectral setup as LB observations.

2.2. Data Reduction

Bands 3 and 4 observations were calibrated with the ALMA pipeline in CASA 6.4.1.12 (CASA Team et al. 2022), and Band 7 observations with the ALMA pipeline in CASA 6.5.4.9. The data reduction followed the standard procedures adopted by the DSHARP collaboration (Andrews et al. 2018). For each execution block, channels containing any line emissions were first flagged from the data when present, and the data was averaged in time to 6 seconds and in frequency over 8 channels.

Self-calibration was then performed in CASA version 6.5.1.23, beginning with the SB data. The SB executions were then concatenated with LB executions and self-calibrated together. All execution blocks were aligned in the u - v plane to the phase center of the LB execution with highest SNR using the exoALMA visibility-alignment tools (Loomis et al. 2025). To boost the signal-to-noise ratio (SNR), we combined scans, spectral windows, and polarizations when computing gain solutions using `gaincal`. The images are reconstructed using `tclean` with a threshold of 3σ and a cell size of tenth the synthesized beam. We employed the Multi-term (Multi-Scale) Multi-Frequency Synthesis deconvolver (`mtmfs`) (Rau & Cornwell 2011) with deconvolution scales of [0, 1, 2, 4, 8] beam sizes and `nterms` = 2. We adopted `briggs` weighting with `robust` = 0.5.

For Band 3 data, three rounds of phase-only self-calibration were executed with progressively shorter solution intervals (`solint` = inf, 300 sec, 100 sec), followed by one round of amplitude calibration with `solint` = inf. The peak SNR was improved by 42% after the self-calibration. A final phase self-calibration with `solint` =

Table 1. Observation and Image Summary

ALMA Band	Program ID	PI	Obs.Freq [GHz]	Synthesized Beam Size [arcsec]	RMS Noise [$\mu\text{Jy Beam}^{-1}$]	Peak SNR
Band 3	2022.1.00315.S	Ruobing Dong	89.54 - 105.48	0.095×0.081	5.99	60
Band 4	2022.1.00315.S	Ruobing Dong	137.04 - 152.99	0.081×0.049	7.41	80
Band 6	2015.1.00192.S	Gerrit van der Plas	215.94 - 235.18	0.056×0.051	20.90	55
	2017.1.01578.S	Jozua de Boer	216.30 - 235.12			
Band 7	2022.1.00315.S	Ruobing Dong	335.55 - 351.50	0.059×0.050	24.99	133
	2023.1.00108.S	Xiaoyi Ma	335.55 - 351.50			

Note: Column 1: ALMA Band; Column 2: ALMA program ID. For Band 3 and 4 observations, SB and LB executions come from the same ALMA program. For Band 6 and 7 observations, SB and LB come from different programs. Band 6 uses SB from 2015.1.00192.S and LB from 2017.1.01578.S. Band 7 uses SB from 2023.1.00108.S and LB from 2022.1.00315.S; Column 3: PI of the ALMA project; Column 4: Observation Frequency range covering all spectral windows; Column 5: Synthesized beam (FWHM) of the final image; imaging details in 2.2; Column 6: RMS noise for the image; Column 7: Peak SNR.

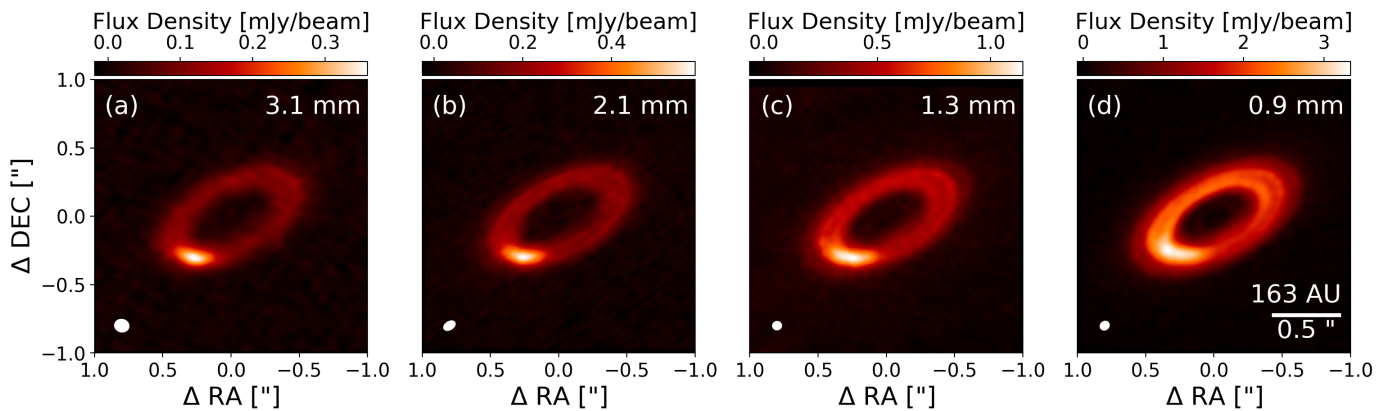


Figure 1. ALMA continuum images at 3.1 mm (a), 2.1 mm (b), 1.3 mm (c), and 0.9 mm (d). The synthesized beam size (peak SNR) is $0.095 \times 0.081''$ (60), $0.081 \times 0.049''$ (80), $0.056 \times 0.051''$ (55), and $0.059 \times 0.050''$ (133) from panel (a) to (d). The fits files are available in the online article.

inf was applied to the concatenated dataset, also combining different scans, spectral windows and polarizations. We did not apply amplitude self-calibration because it did not significantly improve the SNR. The final image has SNR ~ 60 and a synthesized beam of $0.095 \times 0.081''$.

For the Band 4 data, four rounds of phase-only self-calibration were performed with solution intervals of `solint = inf, 300 sec, 100 sec, and 60 sec`, followed by one round of amplitude self-calibration with `solint = inf`. The peak SNR improved by 60% after the self-calibration. We did not perform self-calibration on the final concatenated Band 4 dataset, as it did not significantly improve the SNR and instead reduced the effective angular resolution. The final image has SNR ~ 80 and a synthesized beam of $0.081 \times 0.049''$.

For the Band 7 data, five rounds of phase-only self-calibration were performed with solution intervals of

`solint = inf, 300 sec, 100 sec, 60 sec and 20 sec`. We did not apply amplitude self-calibration because it improved SNR by $< 5\%$. The peak SNR improved by 168% after the self-calibration. Since self-calibration yielded negligible SNR gains and required extensive flagging, we did not apply it to the concatenated dataset. The final image has SNR ~ 133 and a synthesized beam of $0.059 \times 0.050''$.

3. RESULTS

In this section, we present the continuum images across four ALMA bands (§3.1), and characterize the morphology of the arc across wavelength with visibility modeling (§3.2).

3.1. Images

The reconstructed images at all four wavelengths are shown in Figure 1. Rayleigh-Jeans brightness temperature maps are presented in Figure 9, shown both at the native resolution and convolved to a common beam matched to the largest synthesized beam among the four wavelengths ($0.095 \times 0.081''$). At 3.1 and 2.1 mm, the emission reveals two rings with a bright arc on the southeastern side of the outer ring. At 1.3 and 0.9 mm, the higher angular resolution observation resolves the disk into three rings, with a bright arc situated between the two narrower rings. The background rings and gaps show the characteristic “double-gap, triple-ring” structures previously seen in the outer disk of a number of systems, such as TW Hya, HD 169142, AS 209, DoAr 25, Elias 2-20, and in RU Lup (ALMA Partnership et al. 2015; Andrews et al. 2016; Pérez et al. 2019; Huang et al. 2018). Such features may indicate the presence of a super-Earth in the middle ring (Dong et al. 2017, 2018a; Bae et al. 2017).

HD 34282 had previously been imaged at lower resolution ($0.17 \times 0.10''$) at 0.9 mm (van der Plas et al. 2017). They modeled the emission with constant-surface-brightness rings on top of the faint broad background ring and a 2D Gaussian arc centered at $r_{\text{arc}} \simeq 0.43''$ and $\theta_{\text{arc}} \simeq 18^\circ$. The azimuthal angle θ is defined in the deprojected disk plane, measured from the red-shifted side of the disk major axis increasing counterclockwise. We define θ_{arc} as the azimuthal location of the arc center. Higher-resolution imaging at 0.9 mm ($0.067 \times 0.054''$) from exoALMA (Curone et al. 2025), with a resolution comparable to our data, resolves three rings and recovers an arc located at $r_{\text{arc}} \simeq 0.45''$ and $\theta_{\text{arc}} \simeq 20^\circ$, consistent with the result of van der Plas et al. (2017).

Figure 2 shows the deprojected azimuthal intensity profiles evaluated at the arc radius r_{arc} at each wavelength listed in Table 3, as obtained from parametric $\{u, v\}$ -plane fitting with *galario* (Tazzari et al. 2018) (see Appendix B). The profiles are extracted using the disk inclination, position angle, and center offsets obtained from the *galario* fit, and reveal pronounced wavelength-dependent morphology. We convolve all images to a common synthesized beam ($0.095 \times 0.081''$; Band 3 beam; see the lower panel of Figure 9) to enable a fair comparison of the profiles (dashed lines in Figure 2) across wavelengths. The arc-to-ring contrast increases with wavelength in these common beam profiles: contrast = 1.5, 2.0, 2.8 and 3.5 at 0.9, 1.3, 2.1 and 3.1 mm, respectively, similar to PDS 70 (Doi et al. 2024). The arc also becomes azimuthally narrower at longer wavelengths. The arc peak shifts from 0.9 to 1.3 mm, but

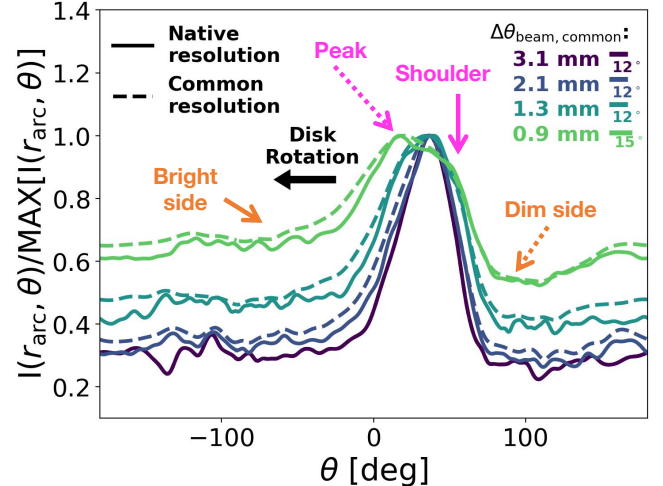


Figure 2. Normalized azimuthal brightness profiles at r_{arc} (Table 3) after deprojection using the geometry in Appendix B. The disk-plane azimuth θ is measured from the red-shifted major axis and increases counterclockwise. Solid curves show profiles from the native-resolution images; dashed curves are from images convolved to a common $0.095 \times 0.081''$ beam (Band 3). The azimuthal resolution, $\Delta\theta_{\text{beam,common}}$, is defined as the tangential FWHM of the deprojected common beam at the arc peak. The black arrow marks clockwise disk rotation (de Boer et al. 2021). The 0.9 mm profile shows a sharp peak with a leading-side shoulder (pink arrows) and asymmetric baselines (orange arrows).

remains consistent at longer wavelengths. Quantitative measurements of the arc azimuthal location and width will be reported in §3.2 and discussed in §4.3.

The arc has a different shape at 0.9 mm compared to longer wavelengths. The azimuthal profile in Figure 2 exhibits a shallow shoulder (pink solid arrow) on the leading side of the arc relative to the disk rotation followed by a sharper peak (pink dashed arrow), whereas the longer-wavelength profiles are closer to a Gaussian shape. The portion of the background ring on the near-side (southwest; orange dashed arrow) is dimmer than the far-side (northeast; orange solid arrow) at both 1.3 and 0.9 mm, and is most pronounced at 0.9 mm.

3.2. Measurement of the Arc Morphology

To facilitate comparison with theoretical predictions of dust trapping (§4.3), we measure the azimuthal position and width of the arc at each wavelength. Due to the complex arc morphology, it is difficult to define a single parametric model that fits the data across all bands (Figure 10; Appendix B), so we instead determine the arc peak and width directly from its azimuthal brightness profile.

Since the arc lies on top of bright rings, its peak and width can be biased by the underlying axisymmetric emission. To minimize this contamination, we follow a procedure similar to Curone et al. (2025) to separate the axisymmetric disk emission from the localized arc. The workflow has three steps:

1. We fit a parametric `galario` visibility model to determine the disk geometry (PA, inclination i), phase-center offsets ($\Delta\alpha, \Delta\delta$), and the arc radius (r_{arc}) at each wavelength. The visibilities are modeled with three Gaussian rings and a 2D Gaussian arc. Further details are provided in Appendix B.
2. We deproject the visibilities using the parameters from step 1 (listed in Table 3) and use `frank` (Jennings et al. 2020) to reconstruct a non-parametric axisymmetric radial intensity profile in logarithmic space on a radial grid with $N = 400$ points. The hyper-parameters are set to $\alpha = 1.3$ and $w_{\text{smooth}} = 0.01$, where α defines the effective signal-to-noise threshold beyond which the data are excluded from the fit, and w_{smooth} suppresses noisy oscillations. We set $R_{\text{max}} = 3''$ to encompass all possible extended emission, such that `frank` assumes zero emission beyond R_{max} . The resulting `frank` model is sampled at the same (u, v) coordinates as the observations to generate synthetic model visibilities. Residual visibilities are obtained by subtracting these synthetic visibilities from the observed ones and imaged using the CASA `tclean` algorithm.
3. We subtract the `frank` model from the visibilities, image the residuals, and measure the arc peak location and full width at half maximum (FWHM) from the deprojected residual profile evaluated at r_{arc} .

Figure 3 shows the `frank` residual maps at 3.1, 2.1, 1.3, and 0.9 mm. At all wavelengths, a bright non-axisymmetric residual is detected on the southeast side of the disk, tracing the localized arc, with peak SNR of 40, 45, 27, and 43 at 3.1, 2.1, 1.3, and 0.9 mm, respectively. There are also low-level, nearly axisymmetric negative residuals associated with the arc located at r_{arc} . Since the `frank` model only includes the azimuthally averaged (axisymmetric) component, the flux of the localized arc is redistributed evenly around the ring in the model. Subtracting this model therefore produces a positive residual at the arc location and a small negative residual along the rest of the ring, which reduces the peak SNR of the arc.

Table 2. Measured arc peak azimuth and azimuthal width (FWHM). Quoted uncertainties are 1σ values estimated from bootstrap resampling.

Wavelength	$\theta_{\text{peak,arc}} [^\circ]$	$\Delta\theta_{\text{FWHM,arc}} [^\circ]$
3.1 mm	35.0 ± 2.2	37.1 ± 1.4
2.1 mm	39.2 ± 1.9	50.0 ± 0.7
1.3 mm	38.3 ± 2.9	57.0 ± 0.9
0.9 mm	23.1 ± 2.6	65.8 ± 0.7

At 0.9 and 1.3 mm, additional positive and negative residuals appear in the narrow rings at $r \sim r_{\text{arc}}$, indicating that the rings are dimmer on the near side and brighter on the far side. This asymmetry within the ring is also evident in the deprojected azimuthal brightness profiles (Figure 2), where the portion of the ring on near-side (southwest) is fainter than the far-side (northeast) at both wavelengths indicated by the orange arrows on the 0.9 mm curve. In addition, an extended arc-like positive residual is detected on the near side of the inner disk at 0.9 mm (arrow in Figure 3d). These features are unlikely to affect our analysis of the arc and are discussed further in §5.

To ensure that differences in beam size do not bias the comparison between bands, we convolve all residual images to a common $0.095 \times 0.081''$ beam (the Band 3 beam). We then deproject each residual image into polar coordinates, $I_{\text{res}}(r, \theta)$, as shown in the top row of Figure 4. At each wavelength, we extract an azimuthal profile at the arc radius r_{arc} (Table 3; black dashed line in Figure 4), shown as the cyan curve in the lower panels of Figure 4.

To isolate the arc emission, we estimate a local background directly from the azimuthal residual profile at the arc radius. We use the profile from the arc-free side, corresponding to the region located 180° away from the arc peak as a reference background (green line in Figure 4), under the assumption that it samples the same underlying axisymmetric emission without contribution from the arc. We subtract this background profile point-by-point from the arc-side residual profile, thereby correcting for the artificial negative baseline introduced when the localized arc biases the `frank` reconstruction. The resulting baseline-corrected profile (blue line in Figure 4) is then used to measure the azimuthal location and width of the arc.

We estimate the statistical uncertainties of the arc peak location and azimuthal width using a bootstrap approach for 500 realizations. In each realization, we perturb the residual azimuthal profile $I_{\text{res}}(r_{\text{arc}}, \theta)$ by adding Gaussian noise with a standard deviation equal to the

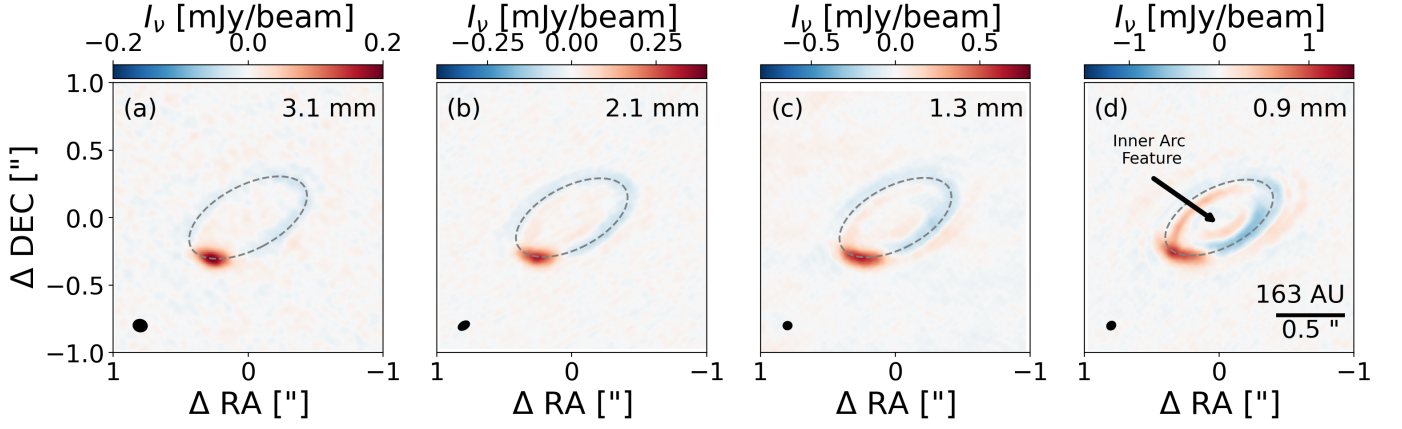


Figure 3. Residual map generated by subtracting the `frank` model from the data at 3.1 mm (a), 2.1 mm (b), 1.3 mm (c), and 0.9 mm (d). The synthesized beam is indicated by the ellipse in the lower left corner. The arc radius r_{arc} is indicated by the dashed gray line. At 0.9 mm, a faint arc-like positive residual is visible at $r \sim 0.17''$ (panel d; arrow).

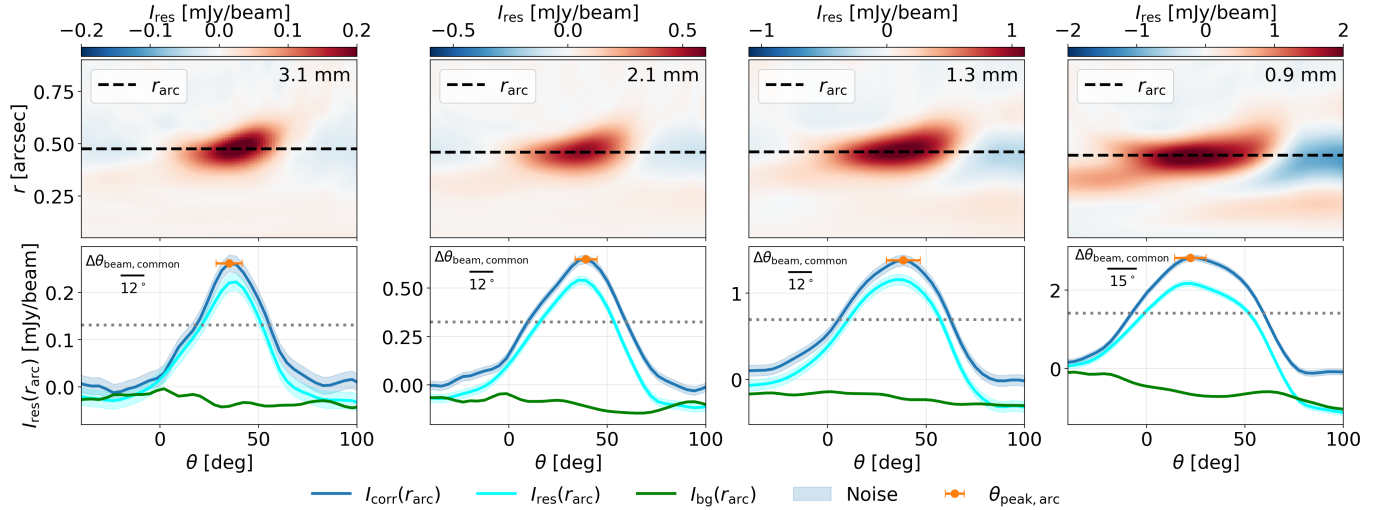


Figure 4. Top: Residual maps (Figure 3) convolved to a common Band 3 beam ($0.095 \times 0.081''$) and deprojected for comparison across 3.1, 2.1, 1.3, and 0.9 mm (left to right). The horizontal dashed line marks r_{arc} . Bottom: Azimuthal profiles of the top panels at r_{arc} (Table 3). Cyan shows the raw residual I_{res} , green is the opposite-sector background I_{bg} , and blue is the background-corrected profile I_{corr} ; the shaded region indicates $\pm 3\sigma$ noise. The orange marker marks the peak $\theta_{\text{peak,arc}}$ with 3σ uncertainty. The horizontal dotted line indicates the half-maximum level in I_{corr} , and the black bar (top left) indicates the effective azimuthal beam $\Delta\theta_{\text{beam,common}}$ at the arc peak. The arc is fully resolved in the azimuthal direction at all wavelengths.

measured map RMS listed in Table 1, re-estimate and subtract the baseline profiles, and then re-measure the peak location $\theta_{\text{peak,arc}}$ and azimuthal width $\Delta\theta_{\text{FWHM,arc}}$ from the noise-perturbed profile. The uncertainties are taken to be the standard deviations of the resulting bootstrap distributions of $\theta_{\text{peak,arc}}$ and $\Delta\theta_{\text{FWHM,arc}}$.

The resulting arc locations and widths are listed in Table 2 and plotted in Figure 6. The measured FWHM decreases monotonically from $\sim 65.8 \pm 0.7^\circ$ at 0.9 mm to $\sim 37.1 \pm 1.4^\circ$ at 3.1 mm. The azimuthal peak shifts by $\sim 15 \pm 4^\circ$ between 0.9 and 1.3 mm, while the relative shifts

among the three longer wavelengths remain undetected ($\lesssim 4^\circ$) within $\sim 1 \sigma_{\theta_{\text{peak,arc}}}$.

The measured azimuthal widths in the common-beam images range from 37° to 66° from 3.1 mm to 0.9 mm, more than three times larger than the effective azimuthal beam sizes of 12° to 15° (Figure 2), indicating that the arc is azimuthally resolved.

The deprojected radial profiles of the residual image at the peak azimuth of $I_{\text{res}}(r_{\text{arc}}, \theta)$, are shown in Figure 5. At 0.9, 1.3, and 2.1 mm, the radial FWHM of the arc is $> 2\times$ the beam, while at 3.1 mm, it is only $1.5\times$

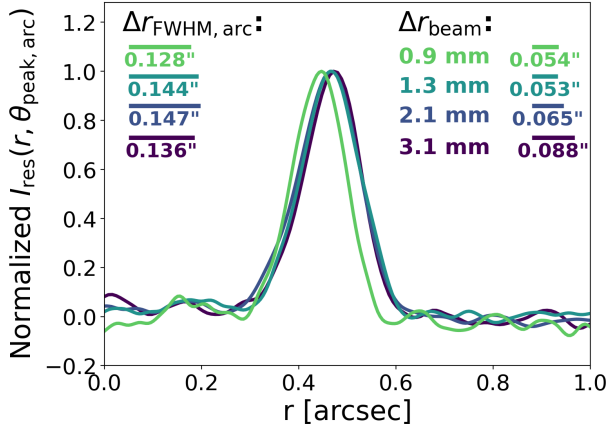


Figure 5. Radial profiles of the normalized residual intensity, $I_{\text{res}}(r, \theta_{\text{peak,arc}})$, extracted at the azimuthal peak of the arc for all four wavelengths, measured from the native-resolution images. The effective beam FWHM at each wavelength, Δr_{beam} , is listed in the upper right. The FWHM of the arc, $\Delta r_{\text{FWHM,arc}}$, is listed in the upper left corner. The arc is only marginally resolved in the radial direction at 3.1 mm ($\Delta r_{\text{FWHM,arc}} = 1.5\Delta r_{\text{beam}}$), but is better resolved at shorter wavelengths ($\Delta r_{\text{FWHM,arc}} > 2\Delta r_{\text{beam}}$).

the beam. Since the arc is azimuthally well resolved, the marginal radial resolution at 3.1 mm primarily averages the emission over a narrow radial range and should not significantly bias $\theta_{\text{peak,arc}}$ or $\Delta\theta_{\text{FWHM,arc}}$, unless the azimuthal profile changes rapidly with radius on scales comparable to the beam.

4. MULTI-WAVELENGTH ANALYSIS

In this section, we estimate the optical depth (§4.1) and spectral index (§4.2) of the observations, and compare the observations with theoretical predictions to assess the consistency of the observed features with a dust-trapping vortex model (§4.3).

4.1. Optical Depth

The observations reveal changes in the arc morphology with wavelength. The observed morphology traces the dust density distribution in the midplane only if the emission is optically thin; otherwise, the emission becomes also sensitive to the temperature distribution. We therefore first estimate the optical depth at each wavelength to determine whether the continuum reliably probes the dust distribution before testing dust-trapping models. We consider emission to be optically thin for optical depth $\tau_{\nu} \lesssim 0.5$, marginally optically thick for $\tau_{\nu} \sim 1$, and optically thick for $\tau_{\nu} \gtrsim 2$.

We estimate τ_{ν} at each wavelength using a toy model based on the Eddington-Barbier approximation in an isothermal slab (Birnstiel et al. 2018) assuming local thermodynamic equilibrium. If we only consider absorption opacity, the optical depth is

$$\tau_{\nu} = -\ln \left[1 - \frac{I_{\nu}}{B_{\nu}(T_{\text{dust}})} \right]. \quad (1)$$

where I_{ν} is the observed surface brightness at frequency ν , and T_{dust} is the dust temperature. We adopt T_{dust} as the midplane temperature from the 2D thermal structure inferred from multiple molecular tracers (Galloway-Sprietsma et al. 2025), assuming the dust and gas are thermally coupled in the disk midplane. At the arc radius, $T_{\text{dust}} = 29.6 \pm 0.1$ K. The quoted error reflects only propagated statistical uncertainties and excludes systematics (e.g., emitting-height/vertical-structure assumptions). For the purpose of classifying the emission from the arc as optically thin versus thick, a moderate temperature offset does not change our qualitative conclusions. For example, a ± 5 K change in T_{dust} would alter τ_{ν} by ~ 25 -30% in the arc. As azimuthal temperature variations potentially induced by a vortex are expected to be small (Temmink et al. 2025), we adopt a constant dust temperature with azimuth.

The azimuthal profiles of the absorption optical depth are shown in Figure 7. The solid curves show τ_{ν} estimated directly from the images. At 3.1, 2.1, 1.3, and 0.9 mm, we measure $\tau_{\nu} \approx 0.08$, 0.10, 0.19, and 0.40 in the ring, and $\tau_{\nu} \approx 0.25$, 0.41, 0.50, and 0.77 in the arc, respectively.

The beam dilution makes the unresolved or marginally resolved features appear fainter than their intrinsic brightness, leading to an underestimate of τ_{ν} . This effect is expected to be the most significant in Band 3, where the beam is the coarsest and the intrinsic dust concentration is likely the most compact. Although the arc is azimuthally resolved, it is only marginally resolved radially at Band 3, as shown in Figure 5. As a result, the image-based estimates of τ_{ν} likely represent lower limits on the intrinsic optical depth of the arc.

To test this effect, we use the best-fit `galario` models (Appendix B), which are fitted directly in the visibility plane and therefore account for beam convolution, to carry out an additional optical depth estimate at 3.1 and 2.1 mm. The results are shown as dot-dashed curves in Figure 7. We restrict this analysis to 3.1 and 2.1 mm because only at these wavelengths does the `galario` model reproduce the data well (Figure 10).

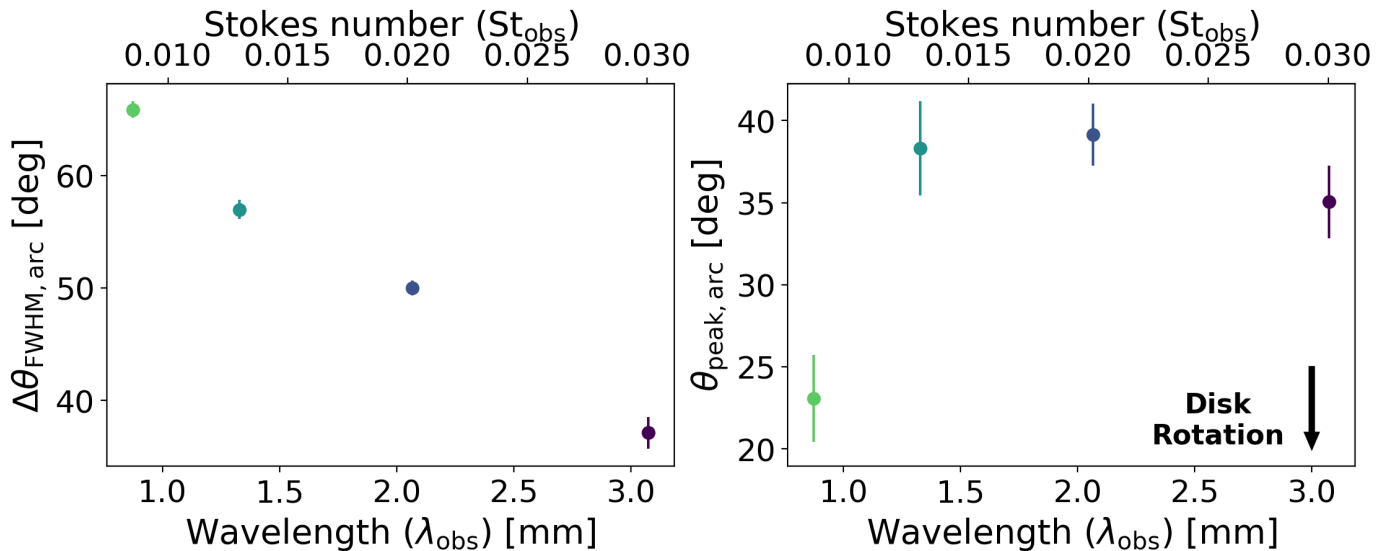


Figure 6. Azimuthal full width at half maximum of the arc, $\Delta\theta_{\text{FWHM,arc}}$ (left), and azimuthal peak location, $\theta_{\text{peak,arc}}$ (right), measured from the baseline-corrected azimuthal profiles of the **frank** residuals (I_{corr} ; bottom row of Figure 4). The measurements are listed in Table 2. The four points correspond to $\lambda_{\text{obs}} = 0.9, 1.3, 2.1,$ and 3.1 mm, with observed Stokes numbers $\text{St}_{\text{obs}} = 0.008, 0.012, 0.020,$ and 0.030 , respectively. Error bars indicate the statistical uncertainties estimated via bootstrap resampling.

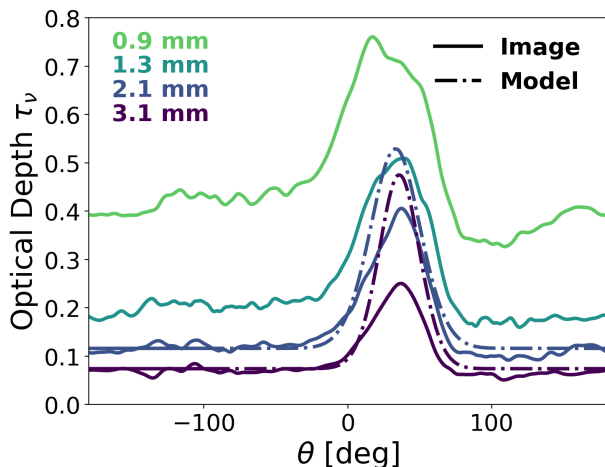


Figure 7. Azimuthal optical depth profiles across the arc. Solid curves show τ_ν measured directly from the images at all four wavelengths, and dot-dashed curves show τ_ν from the best-fit **galarío** parametric models at 3.1 and 2.1 mm, as only the 3.1 and 2.1 mm models reproduce the data well (Figure 10).

At 3.1 mm, the model yields $\tau_\nu \approx 0.47$ at the arc peak, which is higher than $\tau_\nu \approx 0.25$ from the image, consistent with the effect of beam dilution. The ring has $\tau_\nu \approx 0.08$ in both cases. At 2.1 mm, the model gives $\tau_\nu \approx 0.53$ at the arc peak, again higher than the image-based estimate ($\tau_\nu \approx 0.41$), while the ring has $\tau_\nu \approx 0.12$. Even though the arc is radially resolved at 2.1 mm (Figure 5), beam convolution and blending with the underlying ring still suppress the ob-

served peak intensity, so the image-based τ_ν underestimates the intrinsic value recovered by **galarío**. We therefore adopt the model-based optical depths as fiducial estimates at Band 3 and 4. These values indicate that the arc remains intrinsically optically thin in both bands under a pure-absorption assumption even after accounting for beam dilution, while the surrounding ring is more optically thin. However, until higher-resolution observations are available, we cannot formally exclude the possibility that the arc consists of unresolved optically thick clumps with a beam filling factor smaller than unity, which could reproduce the observed optically thin, beam-averaged emission (Dullemond et al. 2018).

At the other extreme, an upper limit on the absorption optical depth at 3.1 and 2.1 mm can be derived by assuming the Band 7 emission is optically thick at the arc location, and adopting the corresponding brightness temperature T_b (computed using the full Planck function) as the mid-plane physical dust temperature. Under this assumption, $\tau_\nu \sim 0.45$ at 3.1 mm and $\tau_\nu \sim 0.82$ at 2.1 mm, in which the emission is still (marginally) optically thin.

Dust scattering at millimeter wavelengths suppresses the emergent intensity for a given extinction optical depth (Zhu et al. 2019; Liu 2019). We estimate optical depths including scattering for a given single-scattering albedo ω_ν by inverting the relation between $\chi_\nu \equiv I_\nu/B_\nu$ and τ_ν (Equation 11 in Zhu et al. (2019)). We adopt $\chi_\nu \simeq 0.378$ at 3.1 mm and $\chi_\nu \simeq 0.411$ at 2.1 mm for the

arc, measured from the best-fit `galarío` models. While ω_ν remains poorly constrained in HD 34282, larger ω_ν implies a stronger suppression of the emergent intensity and therefore requires a larger τ_ν to reproduce the observed χ_ν . Observational constraints generally suggest that disk albedos can reach $\omega_\nu \lesssim 0.8$ (Ueda et al. 2020; Yoshida et al. 2025). For this upper end of plausible albedos, we infer $\tau_\nu \lesssim 1.42$ at 3.1 mm and $\tau_\nu \lesssim 1.67$ at 2.1 mm for the arc, and $\tau_\nu \lesssim 0.19$ at 3.1 mm and $\tau_\nu \lesssim 0.30$ at 2.1 mm for the ring. For a representative albedo of $\omega_\nu = 0.7$, the ring remains optically thin, while the arc is (marginally) optically thin at the two wavelengths.

At shorter wavelengths, the similar peak Rayleigh-Jeans brightness temperatures at the arc in Bands 6 (9.7 ± 0.2 K) and 7 (11.6 ± 0.1 K) (Figure 9) suggest emission approaching optically thick at Band 7. The derived optical depth ($\tau_\nu \sim 0.77$) may therefore be underestimated if dust scattering reduces the observed intensity, implying that the intrinsic optical depth could be higher.

4.2. Spectral Index Distributions

We measure the spectral index of the observed intensity as

$$\alpha = \frac{\ln(I_{\nu_1}/I_{\nu_2})}{\ln(\nu_1/\nu_2)} \quad (2)$$

where I_{ν_1} and I_{ν_2} are the intensities at frequencies ν_1 and ν_2 . We use the data at 3.1 mm and 2.1 mm (Band 3 and 4) to compute α , as these bands are most likely to be optically thin (§4.1), and more reliable tracers of the dust distribution. Prior to this, we align both images to a common center using the position offsets derived in Appendix B, and convolve them to a common beam as $0.095 \times 0.081''$ (Band 3 beam). We compute the spectral index only for regions with SNR > 15 in both bands. The resulting $\alpha_{\text{B4,B3}}$ map is shown in the left panel in Figure 8.

The spectral index uncertainties include contributions from the image RMS noise and the absolute flux calibration. We adopt a 5% absolute flux-calibration uncertainty for both bands (Cortés et al. 2025). The resulting uncertainty map, $\sigma_{\alpha_{\text{B4,B3}}}$, is shown in the middle panel of Figure 8. The spectral index reaches its minimum at the arc, with $\alpha_{\text{B4,B3}} = 2.48 \pm 0.18$, whereas the surrounding ring at r_{arc} has a higher mean value of $\alpha_{\text{B4,B3}} \simeq 3.11 \pm 0.25$, with a peak value exceeding 3.5.

We also compute the spectral index of the isolated arc emission using the peak intensities of the baseline-corrected profiles (I_{corr} ; Figure 4), obtaining $\alpha_{\text{B4,B3}}^{\text{arc}} =$

2.29 ± 0.18 , consistent within uncertainties with the value measured from the observed intensity, indicating that contamination from the underlying ring emission does not significantly affect the spectral index estimate.

Since the arc is not fully resolved radially at 3.1 mm as shown in Figure 5, beam smearing can dilute the peak intensity and bias α locally. To assess this effect, we also compute α from the best-fit `galarío` model images as shown in the right panel of Figure 8. In the model, $\alpha_{\text{B4,B3}}$ reaches values as low as ~ 1.92 within the arc, while remaining ~ 2.98 in the background.

In vortices, dust is expected to grow rapidly to larger sizes than in the surrounding disk. A lower α at the arc may indicate larger grains compared to the background disk (Birnstiel et al. 2013; Testi et al. 2014; Birnstiel 2024), consistent with dust-trapping.

When dust scattering is included, the interpretation of α becomes degenerate. The peak value of $\alpha \gtrsim 3.5$ in the ring is consistent with optically thin emission from small grains (e.g., $\lesssim 100 \mu\text{m}$). The mean value of $\alpha \sim 3$ across the ring may reflect spatial variations in the dust population or optical depth. Meanwhile, the reduced α observed in the arc can arise either from optically thick emission or from optically thin emission dominated by larger grains (Zhu et al. 2019; Liu 2019). In the former case, the enhanced optical depth may be due to dust growth to sizes greater than a millimeter, or a concentration of a very large amount of dust, which are not mutually exclusive. Both scenarios imply that the arc hosts a higher dust surface density and/or larger grain sizes than the surrounding background emission. This is consistent with an enhanced dust concentration and grain growth expected in dust-trapping vortices (Birnstiel et al. 2013; Li et al. 2020).

4.3. Evidence for Dust Trapping

In this section, we assess the dust-trapping hypothesis for the vortex candidate by comparing the wavelength dependence of the arc with theoretical predictions. The azimuthal width and peak shift are examined in §4.3.1 and §4.3.2, respectively.

4.3.1. Azimuthal Width

Both analytical models and numerical simulations predict that larger grains traced by longer-wavelength emission should be more tightly confined azimuthally within a dust-trapping vortex than smaller grains (Birnstiel et al. 2013; Lyra & Lin 2013). This is the result of size-dependent gas-dust coupling. As larger particles

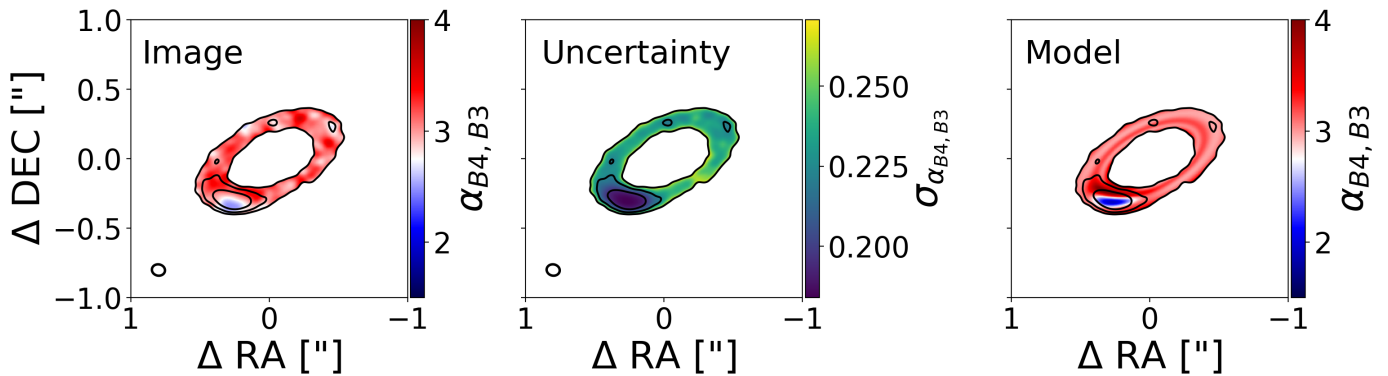


Figure 8. Left: Observed spectral index map between ALMA Bands 3 and 4. The common resolution of $0.095 \times 0.081''$ (the Band 3 beam) is shown by the ellipse in the lower-left corner; black contours trace the Band 3 continuum emission. Middle: Corresponding 1σ uncertainty map, including contributions from the image RMS noise and the absolute flux-calibration uncertainties. Right: Spectral index map between Bands 3 and 4 computed from the best-fit `galario` models (Appendix B).

are more weakly coupled to the gas, they drift more efficiently toward pressure maxima, resulting in a narrower azimuthal concentration of dust.

Our data follow this prediction. The measured azimuthal widths decrease systematically with wavelength (Figure 6), consistent with size-dependent trapping of larger grains. This trend remains after beam matching and subtraction of the axisymmetric component, indicating that it is intrinsic (Figure 2).

While the observed trend may be influenced by the potentially high optical depth at 0.9 and 1.3 mm, it may be less affected at 2.1 and 3.1 mm, where the emission is expected to be at least marginally optically thin (§4.1). In addition, this trend persists when the emission in the background ring is subtracted. The azimuthal FWHM measured from the baseline-corrected `frank` residual profile (Figure 6) decreases from $\Delta\theta_{\text{FWHM,arc}} \approx 50.0 \pm 0.7^\circ$ at 2.1 mm to $\approx 37.1 \pm 1.4^\circ$ at 3.1 mm (Table 2). Since `frank` removes the axisymmetric component, these widths are minimally affected by the underlying ring and provide a robust estimate of the intrinsic arc width.

To further characterize the morphology of the arc in HD 34282, we estimate its aspect ratio using the observed azimuthal FWHM, $\Delta\theta_{\text{FWHM,arc}}$ (Figure 6), and radial FWHM, $\Delta r_{\text{FWHM,arc}}$ (Figure 5), at the three shorter wavelengths, where the arc is well resolved in 2D. We find aspect ratios of 2.7, 3.2, and 4.0 at 2.1, 1.3, and 0.9 mm, respectively, indicating a moderately elongated structure. These values are comparable to other arcs, such as the north and south arcs in MWC 758 (3.1 and 4.0, values derived here from Table 1 of Dong et al. 2018b). The inferred range is also consistent with the

aspect ratios expected for stable vortices (> 2) in analytic models (Lyra & Lin 2013).

4.3.2. Peak Shift

In vortices, the azimuthal trapping location of dust particles depends on their Stokes number, St , which quantifies the degree of dust-gas coupling, and can also be affected by vortex self-gravity. For tightly coupled grains ($St \lesssim 0.1$), dust is trapped close to the pressure maximum and vortex self-gravity is expected to produce negligible azimuthal offsets. For weakly coupled grains, vortex self-gravity can push the dust peak azimuthally ahead of the gas vortex, producing azimuthal shifts in the direction of disk rotation with increasing wavelength (Mittal & Chiang 2015; Baruteau & Zhu 2016).

We now estimate the Stokes number of the dust probed by our observations, St_{obs} . In the Epstein regime,

$$St_{\text{obs}} = \frac{\pi \rho_s a}{2 \Sigma_{\text{gas}}(r_{\text{arc}})}, \quad (3)$$

where a is the grain size, Σ_{gas} is the gas surface density, and ρ_s is the internal grain density. We assume that emission at each wavelength is dominated by a characteristic size $a \sim \lambda_{\text{obs}}/2\pi$ (Draine 2006) and take $\rho_s = 1 \text{ g cm}^{-3}$. We adopt $\Sigma_{\text{gas}}(r_{\text{arc}} = 0.45'') = 2.6 \text{ g cm}^{-2}$ inferred from CO kinematics (Longarini et al. 2025). The Stokes number St_{obs} here refers to an observational quantity associated with the grains dominating the emission at a given wavelength (van der Marel et al. 2021), rather than a unique physical Stokes number of the dust population. We obtained St_{obs} for $\lambda_{\text{obs}} = 3.1, 2.1, 1.3$ and 0.9 mm as shown in Figure 6. This yields $St_{\text{obs}} \lesssim 0.03$ at all four wavelengths, a regime in which theory predicts negligible azimuthal offsets (Baruteau & Zhu 2016).

The observations at $\lambda_{\text{obs}} \geq 1.3$ mm agree with this prediction. The azimuthal positions of the arc at 1.3, 2.1, and 3.1 mm are mutually consistent within $\sim 1\sigma$ (Figure 6). The peak shifts by only $\sim 1 \pm 3^\circ$ between 1.3 and 2.1 mm and by $\sim 4 \pm 3^\circ$ between 2.1 and 3.1 mm.

From 0.9 to 1.3 mm, the arc peak shifts by $\sim 15 \pm 4^\circ$ in the direction opposite to the disk rotation (Figure 6), as inferred from scattered-light imaging and gas kinematics (de Boer et al. 2021; van der Plas et al. 2017). A qualitatively similar behavior has been reported in HD 135344B, where the arc peak shifts by $\sim 50^\circ$ between Band 9 and Band 3, also opposite to the direction of disk rotation (Cazzoletti et al. 2018). Given the very small Stokes numbers in HD 34282, such a large, reversed shift cannot arise from vortex self-gravity and likely reflects other effects, such as optical depth or temperature structure.

5. ADDITIONAL BAND 7 FEATURES

At Band 7 (0.9 mm), we detect an arc-shoulder feature with a large azimuthal offset from the arc seen at longer wavelengths (pink arrows in Figure 2). The origin of this feature is unclear. One possible explanation is azimuthal temperature variation. If the emission is (marginally) optically thick at Band 7 (e.g., with $\tau_\nu \sim 1.1$, van der Plas et al. 2017), the brightness distribution may partly trace the temperature rather than the dust column density. Simulations show that gas perturbations in an anticyclonic vortex co-rotate with the vortex and can displace slightly hotter gas outward and cooler gas inward, producing a downstream temperature enhancement (Lovelace & Romanova 2014).

It is not yet clear whether a comparable effect should occur for the dust. Testing it with the dust emission data presented here will require predictions generated using coupled dust-gas radiative transfer modeling.

Images at 0.9 mm exhibit a localized dimming of two narrow rings on the southwest side of the disk. This is reflected in the deprojected azimuthal brightness at the arc radius (Figure 2), where the portion of the ring at near-side of the arc (orange dashed arrow) is fainter than the far-side (orange solid arrow). The origin of this dim feature is unclear. It could reflect azimuthal temperature variations caused by shadows, or changes in optical depth and scattering geometry that reduce the apparent brightness in dust emission. Additional scattered-light observations probing a potentially misaligned inner disk, combined with radiative transfer modeling, might be helpful to clarify the origin of this feature.

We also detect a faint, azimuthally extended arc at $r \sim 0.17''$ with $\sim 7\sigma$ significance, appearing as an arc-like positive residual in the `frank` residual map (arrow in Figure 3d). This feature is not detected in scattered light data (de Boer et al. 2021; Quiroz et al. 2022), but it lies close to the inner working angle, where sensitivity to small-separation structure is limited. Recent non-redundant masking interferometry has revealed a ring-like component at $r \sim 0.23''$ in the L' band (Vides et al. 2025), broadly comparable to the feature identified here.

6. CONCLUSIONS

We present new ALMA continuum observations of the HD 34282 protoplanetary disk at 0.9, 2.1, and 3.1 mm, together with archival 1.3 mm data, all with sub- $0.1''$ resolution (Figure 1). The disk hosts an inner cavity, and the outer disk shows a characteristic compact double-gap, triple-ring morphology (more pronounced at shorter wavelengths), similar to the pattern found in a number of other disks, such as HL Tau and HD 169142. The disk also shows a prominent arc that is azimuthally resolved at all wavelengths (Figure 2). In the radial direction, its FWHM is $> 2\times$ the beam size at 0.9, 1.3, and 2.1 mm, and $\approx 1.5\times$ the beam size at 3.1 mm (Figure 5). We test the dust-trapping interpretation of the arc by comparing its wavelength-dependent morphology with theoretical predictions. Our main conclusions are:

1. The azimuthal width of the arc decreases monotonically toward longer wavelengths from $65.8 \pm 0.7^\circ$ at 0.9 mm to $37.1 \pm 1.4^\circ$ at 3.1 mm (§4.3.1; Figure 6; Table 2). This trend is consistent with dust trapping (Birnstiel et al. 2013), in which larger grains traced by longer wavelengths (and thus higher Stokes number, St) are more tightly confined azimuthally.
2. The dust in HD 34282 probed by our observations is estimated to have $St_{\text{obs}} \lesssim 0.03$. For such tightly coupled dust, vortex models predict negligible azimuthal peak shifts due to vortex self-gravity (Mittal & Chiang 2015; Baruteau & Zhu 2016). Our 1.3, 2.1 and 3.1 mm measurements are consistent with this expectation (§4.3.2; Figure 6). In contrast, the azimuthal peak differs by $15 \pm 4^\circ$ between 0.9 and 1.3 mm. The peak shifts opposite to the disk rotation as wavelength increases, similar to HD 135344B (Cazzoletti et al. 2018). This behavior may reflect optical-depth or temperature effects.
3. The arc structure at 2.1 and 3.1 mm is well reproduced by parametric `galario` visibility mod-

els consisting of radial Gaussian rings and a 2D Gaussian arc (Appendix B). We estimate the optical depth from both the ALMA images and the `galario` model by comparing the measured brightness temperature with the expected dust temperature. In both cases, the brightness temperature is well below the dust temperature, implying optically thin emission at these wavelengths (§4.1; Figure 7). This conclusion remains valid when dust scattering is included for plausible albedos of $\omega_\nu \simeq 0.7$. However, the arc may be optically thick at 0.9 mm.

4. The 2.1-3.1 mm spectral index within the arc ($\alpha \sim 2.5$) is lower than that in the background rings ($\alpha \sim 3$), potentially suggesting moderately optically thick emission and/or optically thin emission dominated by mm-sized grains in the arc, as predicted by theory (Li et al. 2020) (§4.2; Figure 8).
5. At 0.9 mm we detect additional structure beyond the ring and arc at the arc radius $r_{\text{arc}} = 0.44''$, including an arc-shoulder feature (pink arrows in Figure 2), and a localized dimming of the ring on the southwest side (orange dashed arrow in Figure 2). We also detect a faint, azimuthally extended arc at $r \sim 0.17''$ (arrow in Figure 3d). The origins of these structures are unclear, but they may reflect azimuthal temperature variations and/or optical-depth and scattering effects (§5).

Overall, our observations suggest that the HD 34282 arc traces dust trapping in a long-lived pressure max-

imum, potentially a dust-trapping vortex. A definitive test will require longer-wavelength continuum data to constrain the grain-size distribution, together with high-resolution, high-sensitivity molecular-line kinematics to search for local deviations from Keplerian rotation (Huang et al. 2019).

ACKNOWLEDGEMENTS

We are grateful to an anonymous referee for constructive suggestions that improved our paper. We thank Bin Ren, Eve Lee, Gregory J. Herczeg, Haochang Jiang, John Carpenter, Lile Wang, Milou Temmink, Nagayoshi Ohashi, Shangjia Zhang, and Yangfan Shi for their insightful comments and suggestions, and Logan Francis for providing the processed Band 6 data. This study was supported by the National Key R&D Program of China (Grant No. 2025YFE0123100). This research was enabled in part by support provided by the High-performance Computing Platform of Peking University, and the Digital Research Alliance of Canada (alliance.can.ca). This work was also supported by ADVANCED 149943 and 2024-1.2.8-TÉT-IPARI-CN-2025-00036 grants, which have been implemented with the support provided by the Ministry of Culture and Innovation of Hungary from the National Research, Development and Innovation Fund, financed under the NKKP ADVANCED and 2024-1.2.8-TÉT-IPARI-CN funding schemes. H.B.L. is supported by the National Science and Technology Council (NSTC) of Taiwan (Grant Nos. 113-2112-M-110-022-MY3).

APPENDIX

A. BRIGHTNESS TEMPERATURE IMAGES

We show the Rayleigh-Jeans brightness temperature maps in Figure 9.

B. DISK MODELING WITH GALARIO

In this section, we fit parametric `galario` models to the visibilities at all four wavelengths. For each wavelength, we fit for the position angle (PA), inclination (i), and the offsets between the phase center and disk center, $(\Delta\alpha, \Delta\delta)$. We adopt the global morphological model of Curone et al. (2025) for HD 34282, in which the surface brightness I_ν in disk-plane polar coordinates (r, θ) consists of three axisymmetric Gaussian rings and a 2D Gaussian arc:

$$I(r, \theta) = \sum_{k=1}^3 f_k \exp\left[-\frac{(r - r_k)^2}{2\sigma_k^2}\right] + f_{\text{arc}} \exp\left[-\frac{(r - r_{\text{arc}})^2}{2\sigma_{r,\text{arc}}^2}\right] \exp\left[-\frac{(\theta - \theta_{\text{arc}})^2}{2\sigma_{\theta,\text{arc}}^2}\right] \quad (\text{B1})$$

The amplitudes f_k and f_{arc} are sampled uniformly in log space. The model visibilities, V_{mod} , are generated by Fourier transforming the sky brightness model after projecting it onto the plane of the sky, and then sampling the result at

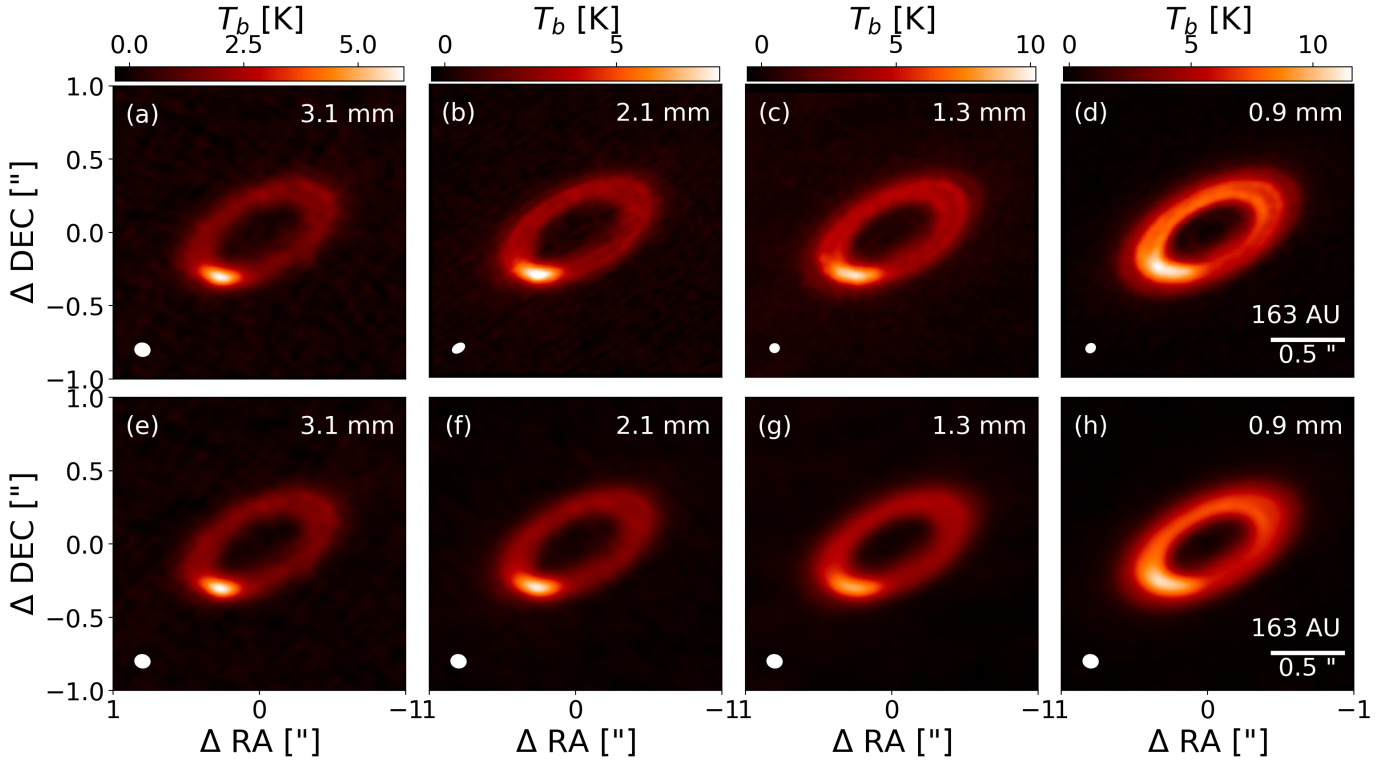


Figure 9. Rayleigh-Jeans brightness temperature maps at (a) 3.1 mm, (b) 2.1 mm, (c) 1.3 mm, and (d) 0.9 mm. The synthesized beam sizes (peak S/N) are $0.095 \times 0.081''$ (60), $0.081 \times 0.049''$ (80), $0.056 \times 0.051''$ (55), and $0.059 \times 0.050''$ (133) from panels (a) to (d), respectively. Panels (e) to (h) show the corresponding maps convolved to a common angular resolution, matched to the largest beam among the four bands ($0.095 \times 0.081''$), which is indicated in each panel.

the observed (u_j, v_j) coordinates:

$$V_{\text{mod}}(u_j, v_j) = \mathcal{F}\{I_\nu(x, y)\}|_{(u_j, v_j)} \quad (\text{B2})$$

We adopt a standard Gaussian likelihood, equivalent to minimizing the weighted complex χ^2 :

$$\ln \mathcal{L} = -\frac{1}{2} \sum_j w_j \left[(\text{Re } V_{\text{data},j} - \text{Re } V_{\text{mod},j})^2 + (\text{Im } V_{\text{data},j} - \text{Im } V_{\text{mod},j})^2 \right] \quad (\text{B3})$$

where $V_{\text{data},j}$ are the observed visibilities and w_j are their corresponding statistical weights. The likelihood is computed directly on the full set of unbinned visibilities. The image pixel scale is chosen to satisfy Nyquist sampling for the observed baselines, and the field of view is set just large enough to enclose the disk emission. This choice preserves the angular resolution across the disk while minimizing computational cost. We sample the posterior distribution of the model parameters (Eq. B3) using a Markov Chain Monte Carlo (MCMC) approach via `emcee` (Foreman-Mackey et al. 2013).

To ensure a robust and efficient exploration of the parameter space, we fit the model with a two-step coarse-to-fine MCMC scheme, similar to the procedure used in Curone et al. (2025). A first coarse run uses uniformly seeded walkers within physically motivated bounds to locate the main posterior modes. A second fine run reinitialized walkers in a tight Gaussian ball around the coarse-run medians ($\sigma = 10^{-4}$ for each parameter in the same units as the corresponding parameter) and resamples with the same likelihood for high-precision posteriors. We start with the high-S/N Band 7 data, then use its posterior medians to initialize independent fits for Bands 3, 4, and 6, allowing band-to-band parameter variations while improving stability and reproducibility.

The best-fit parameters are listed in Table 3. Across all wavelengths, we find consistent geometric parameters, with an inclination of $\sim 60^\circ$ and a position angle of $\sim 117.5^\circ$, in agreement with previous ALMA observations at 0.9 mm

Table 3. Best-fit results from `galarío` for the three-ring plus one-arc model of HD 34282

Parameter	B3 (3.1 mm)	B4 (2.1 mm)	B6 (1.3 mm)	B7 (0.9 mm)
<i>Ring 1</i>				
$\log_{10}(f_1)$ (Jy sr ⁻¹)	8.006 ^{+0.025} _{-0.022}	8.519 ^{+0.013} _{-0.012}	8.9687 ^{+0.0058} _{-0.0069}	9.6028 ^{+0.0030} _{-0.0030}
r_1 (mas)	358 ⁺¹⁹ ₋₂₁	354 ⁺¹¹ ₋₁₂	409 ⁺¹⁶ ₋₂	384.0 ^{+3.9} _{-3.1}
σ_1 (mas)	363 ⁺¹⁵ ₋₁₆	373.8 ^{+9.5} _{-9.1}	405.4 ^{+2.5} _{-2.8}	430.5 ^{+2.0} _{-2.2}
<i>Ring 2</i>				
$\log_{10}(f_2)$ (Jy sr ⁻¹)	8.497 ^{+0.046} _{-0.053}	8.978 ^{+0.027} _{-0.031}	9.385 ^{+0.016} _{-0.015}	10.141 ^{+0.018} _{-0.016}
r_2 (mas)	371.9 ^{+3.0} _{-3.3}	364.2 ^{+2.2} _{-2.5}	347.66 ^{+0.86} _{-0.79}	360.1 ^{+1.1} _{-0.8}
σ_2 (mas)	35.8 ^{+4.0} _{-4.2}	42.9 ^{+2.0} _{-2.2}	42.0 ^{+1.7} _{-1.8}	59.3 ^{+1.9} _{-1.3}
<i>Ring 3</i>				
$\log_{10}(f_3)$ (Jy sr ⁻¹)	8.7059 ^{+0.0068} _{-0.0072}	9.2169 ^{+0.0044} _{-0.0044}	9.7954 ^{+0.0024} _{-0.0025}	10.3207 ^{+0.0043} _{-0.0056}
r_3 (mas)	509.3 ^{+4.7} _{-5.2}	505.0 ^{+2.8} _{-3.1}	486.7 ^{+1.5} _{-1.7}	505.7 ^{+3.2} _{-2.6}
σ_3 (mas)	79.7 ^{+4.6} _{-4.6}	87.7 ^{+2.5} _{-2.4}	108.5 ^{+1.1} _{-1.2}	109.6 ^{+1.3} _{-1.6}
<i>arc</i>				
$\log_{10}(f_{\text{arc}})$ (Jy sr ⁻¹)	9.384 ^{+0.014} _{-0.014}	9.7018 ^{+0.0061} _{-0.0057}	10.0072 ^{+0.0035} _{-0.0036}	10.2565 ^{+0.0034} _{-0.0033}
r_{arc} (mas)	475.1 ^{+2.1} _{-2.1}	459.2 ^{+1.0} _{-1.1}	461.28 ^{+0.71} _{-0.64}	442.13 ^{+0.50} _{-0.40}
$\sigma_{r,\text{arc}}$ (mas)	35.3 ^{+1.1} _{-1.1}	44.21 ^{+0.62} _{-0.69}	49.14 ^{+0.68} _{-0.46}	48.45 ^{+0.39} _{-0.38}
θ_{arc} (deg)	35.77 ^{+0.32} _{-0.40}	33.05 ^{+0.18} _{-0.18}	30.795 ^{+0.078} _{-0.091}	13.77 ^{+0.16} _{-0.18}
$\sigma_{\theta,\text{arc}}$ (deg)	15.18 ^{+0.27} _{-0.27}	18.62 ^{+0.16} _{-0.16}	21.273 ^{+0.089} _{-0.067}	28.90 ^{+0.15} _{-0.16}
<i>Geometry</i>				
Inclination i (deg)	60.109 ^{+0.093} _{-0.097}	59.381 ^{+0.051} _{-0.044}	59.443 ^{+0.0001} _{-0.0001}	59.523 ^{+0.014} _{-0.013}
PA (deg)	117.56 ^{+0.12} _{-0.12}	117.40 ^{+0.07} _{-0.06}	117.905 ^{+0.0001} _{-0.0001}	117.583 ^{+0.015} _{-0.016}
$\Delta\alpha$ (mas)	10.09 ^{+0.76} _{-0.76}	18.91 ^{+0.35} _{-0.35}	-28.85 ^{+0.10} _{-0.12}	29.30 ^{+0.09} _{-0.09}
$\Delta\delta$ (mas)	-11.99 ^{+0.63} _{-0.60}	-25.10 ^{+0.24} _{-0.28}	59.48 ^{+0.08} _{-0.11}	-18.06 ^{+0.06} _{-0.07}

Note. Columns correspond to different observing bands (B3, B4, B6 and B7), while rows list the fitted parameters. For the ring and arc components, we report the median of the marginalized posterior distribution and the corresponding statistical uncertainties from the 16th and 84th percentiles of the MCMC marginalized distributions. The geometry section lists the inclination (i), position angle (PA), and positional offsets ($\Delta\alpha$, $\Delta\delta$) for each band.

(van der Plas et al. 2017; Curone et al. 2025). Figure 10 presents the synthesized images of the best-fit models and the corresponding residuals. At 3.1 and 2.1 mm, the residuals are low and noise-like, indicating that the ring-arc morphology is well reproduced. At 1.3 and 0.9 mm, residual structures at $> 10\sigma$ level remain, suggesting additional substructures not captured by our simple model.

REFERENCES

- ALMA Partnership, Brogan, C. L., Pérez, L. M., et al. 2015, *ApJL*, 808, L3, doi: [10.1088/2041-8205/808/1/L3](https://doi.org/10.1088/2041-8205/808/1/L3)
- Andrews, S. M., Wilner, D. J., Zhu, Z., et al. 2016, *ApJL*, 820, L40, doi: [10.3847/2041-8205/820/2/L40](https://doi.org/10.3847/2041-8205/820/2/L40)
- Andrews, S. M., Huang, J., Perez, L. M., et al. 2018, *The Astrophysical Journal Letters*, 869, L41, doi: [10.3847/2041-8213/aaf741](https://doi.org/10.3847/2041-8213/aaf741)
- Ataiee, S., Pinilla, P., Zsom, A., et al. 2013, *A&A*, 553, L3, doi: [10.1051/0004-6361/201321125](https://doi.org/10.1051/0004-6361/201321125)
- Bae, J., Zhu, Z., & Hartmann, L. 2017, *ApJ*, 850, 201, doi: [10.3847/1538-4357/aa9705](https://doi.org/10.3847/1538-4357/aa9705)
- Baruteau, C., & Zhu, Z. 2016, *Monthly Notices of the Royal Astronomical Society*, 458, 3927, doi: [10.1093/mnras/stv2527](https://doi.org/10.1093/mnras/stv2527)
- Birnstiel, T. 2024, *Annual Review of Astronomy and Astrophysics*, 62, 157, doi: [10.1146/annurev-astro-071221-052705](https://doi.org/10.1146/annurev-astro-071221-052705)
- Birnstiel, T., Dullemond, C. P., & Pinilla, P. 2013, *A&A*, 550, L8, doi: [10.1051/0004-6361/201220847](https://doi.org/10.1051/0004-6361/201220847)
- Birnstiel, T., Dullemond, C. P., Zhu, Z., et al. 2018, *ApJL*, 869, L45, doi: [10.3847/2041-8213/aaf743](https://doi.org/10.3847/2041-8213/aaf743)
- Boccaletti, A., Di Folco, E., Pantin, E., et al. 2020, *A&A*, 637, L5, doi: [10.1051/0004-6361/202038008](https://doi.org/10.1051/0004-6361/202038008)

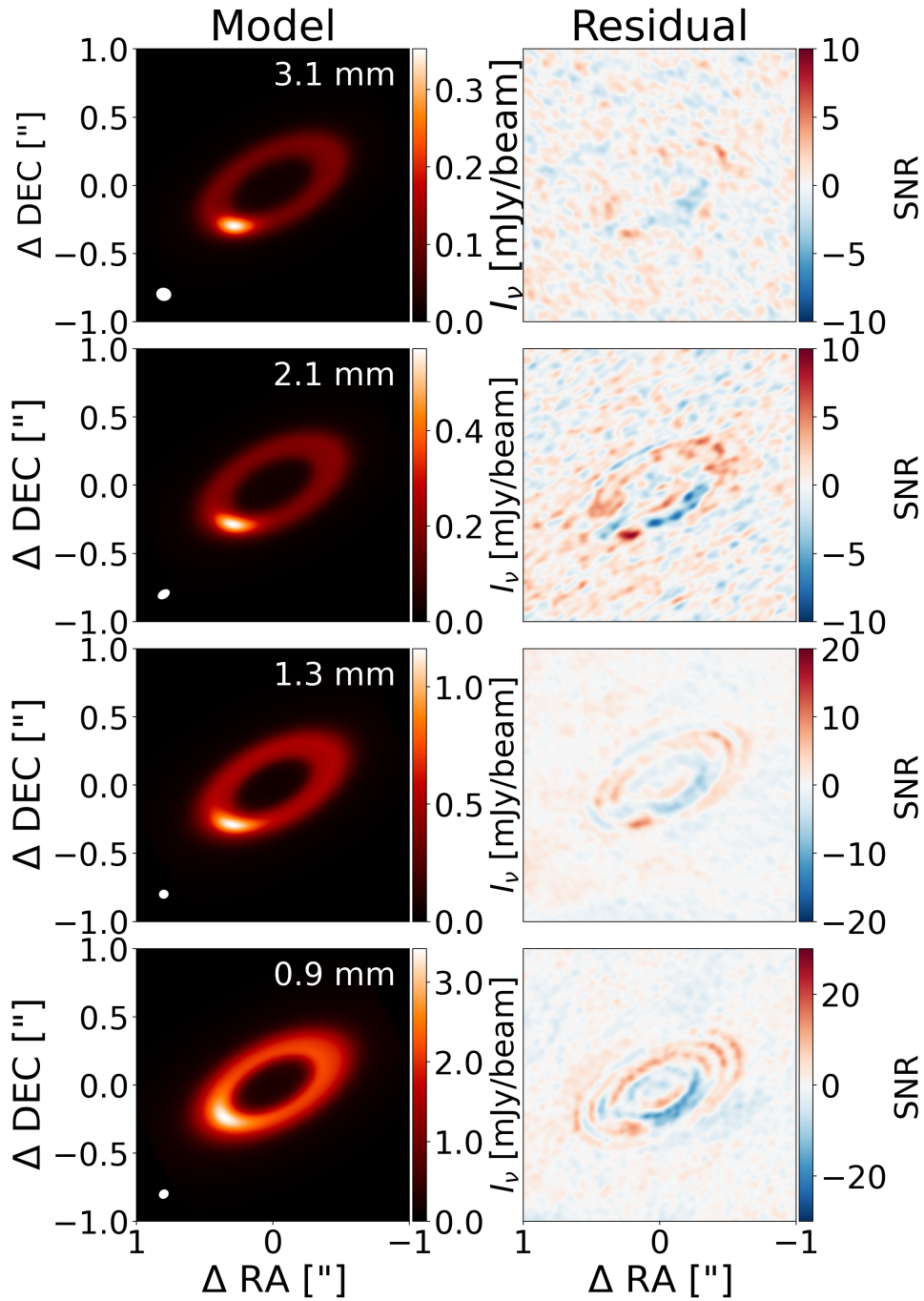


Figure 10. Left: models generated with the best-fit visibility parameters (Table 3) at 3.1, 2.1, 1.3, and 0.9 mm (top to bottom). The synthesized beams are shown as white ellipses. Right: corresponding residual maps in signal-to-noise ratio (SNR).

Boehler, Y., Ricci, L., Weaver, E., et al. 2018, The Astrophysical Journal, 853, 162, doi: [10.3847/1538-4357/aaa19c](https://doi.org/10.3847/1538-4357/aaa19c)

Boehler, Y., Ménard, F., Robert, C. M. T., et al. 2021, A&A, 650, A59, doi: [10.1051/0004-6361/202040089](https://doi.org/10.1051/0004-6361/202040089)

CASA Team, Bean, B., Bhatnagar, S., et al. 2022, PASP, 134, 114501, doi: [10.1088/1538-3873/ac9642](https://doi.org/10.1088/1538-3873/ac9642)

Casassus, S., Wright, C. M., Marino, S., et al. 2015, The Astrophysical Journal, 812, 126, doi: [10.1088/0004-637x/812/2/126](https://doi.org/10.1088/0004-637x/812/2/126)

Casassus, S., Marino, S., Lyra, W., et al. 2019, MNRAS, 483, 3278, doi: [10.1093/mnras/sty3269](https://doi.org/10.1093/mnras/sty3269)

Cazzoletti, P., van Dishoeck, E. F., Pinilla, P., et al. 2018, Astronomy& Astrophysics, 619, A161, doi: [10.1051/0004-6361/201834006](https://doi.org/10.1051/0004-6361/201834006)

- Cimerman, N. P., & Rafikov, R. R. 2023, *MNRAS*, 519, 208, doi: [10.1093/mnras/stac3507](https://doi.org/10.1093/mnras/stac3507)
- Cortés, P., Carpenter, J., Kameno, S., et al. 2025, *ALMA Cycle 12 Technical Handbook*, Tech. rep., Atacama Large Millimeter/submillimeter Array (ALMA), doi: [10.5281/zenodo.14933753](https://doi.org/10.5281/zenodo.14933753)
- Curone, P., Facchini, S., Andrews, S. M., et al. 2025, *ApJL*, 984, L9, doi: [10.3847/2041-8213/adc438](https://doi.org/10.3847/2041-8213/adc438)
- de Boer, J., Ginski, C., Chauvin, G., et al. 2021, *Astronomy & Astrophysics*, 649, A25, doi: [10.1051/0004-6361/201936787](https://doi.org/10.1051/0004-6361/201936787)
- Doi, K., Kataoka, A., Liu, H. B., et al. 2024, Asymmetric dust accumulation of the PDS 70 disk revealed by ALMA Band 3 observations. <https://arxiv.org/abs/2408.09216>
- Dong, R., Li, S., Chiang, E., & Li, H. 2017, *ApJ*, 843, 127, doi: [10.3847/1538-4357/aa72f2](https://doi.org/10.3847/1538-4357/aa72f2)
- . 2018a, *ApJ*, 866, 110, doi: [10.3847/1538-4357/aadadd](https://doi.org/10.3847/1538-4357/aadadd)
- Dong, R., Liu, S.-y., Eisner, J., et al. 2018b, *ApJ*, 860, 124, doi: [10.3847/1538-4357/aac6cb](https://doi.org/10.3847/1538-4357/aac6cb)
- Draine, B. T. 2006, *The Astrophysical Journal*, 636, 1114, doi: [10.1086/498130](https://doi.org/10.1086/498130)
- Dullemond, C. P., Birnstiel, T., Huang, J., et al. 2018, *ApJL*, 869, L46, doi: [10.3847/2041-8213/aaf742](https://doi.org/10.3847/2041-8213/aaf742)
- Flock, M., Ruge, J. P., Dzyurkevich, N., et al. 2015, *A&A*, 574, A68, doi: [10.1051/0004-6361/201424693](https://doi.org/10.1051/0004-6361/201424693)
- Foreman-Mackey, D., Hogg, D. W., Lang, D., & Goodman, J. 2013, *PASP*, 125, 306, doi: [10.1086/670067](https://doi.org/10.1086/670067)
- Francis, L., & van der Marel, N. 2020, *The Astrophysical Journal*, 892, 111, doi: [10.3847/1538-4357/ab7b63](https://doi.org/10.3847/1538-4357/ab7b63)
- Fu, W., Li, H., Lubow, S., Li, S., & Liang, E. 2014, *ApJL*, 795, L39, doi: [10.1088/2041-8205/795/2/L39](https://doi.org/10.1088/2041-8205/795/2/L39)
- Gaia Collaboration, Vallenari, A., Brown, A. G. A., et al. 2023, *A&A*, 674, A1, doi: [10.1051/0004-6361/202243940](https://doi.org/10.1051/0004-6361/202243940)
- Galloway-Sprietsma, M., Bae, J., Izquierdo, A. F., et al. 2025, *The Astrophysical Journal Letters*, 984, L10, doi: [10.3847/2041-8213/adc437](https://doi.org/10.3847/2041-8213/adc437)
- Huang, J., Andrews, S. M., Dullemond, C. P., et al. 2018, *ApJ*, 869, L42, doi: [10.3847/2041-8213/aaf740](https://doi.org/10.3847/2041-8213/aaf740)
- Huang, P., Dong, R., Li, H., Li, S., & Ji, J. 2019, *ApJL*, 883, L39, doi: [10.3847/2041-8213/ab40c4](https://doi.org/10.3847/2041-8213/ab40c4)
- Jennings, J., Booth, R. A., Tazzari, M., Rosotti, G. P., & Clarke, C. J. 2020, *MNRAS*, 495, 3209, doi: [10.1093/mnras/staa1365](https://doi.org/10.1093/mnras/staa1365)
- Kraus, S., Kreplin, A., Fukugawa, M., et al. 2017, *The Astrophysical Journal Letters*, 848, L11, doi: [10.3847/2041-8213/aa8edc](https://doi.org/10.3847/2041-8213/aa8edc)
- Law, C. J., Teague, R., Öberg, K. I., et al. 2023, *ApJ*, 948, 60, doi: [10.3847/1538-4357/acb3c4](https://doi.org/10.3847/1538-4357/acb3c4)
- Li, H., Finn, J. M., Lovelace, R. V. E., & Colgate, S. A. 2000, *ApJ*, 533, 1023, doi: [10.1086/308693](https://doi.org/10.1086/308693)
- Li, Y.-P., Li, H., Li, S., et al. 2020, *The Astrophysical Journal Letters*, 892, L19, doi: [10.3847/2041-8213/ab7fb2](https://doi.org/10.3847/2041-8213/ab7fb2)
- Lin, M.-K. 2012, *MNRAS*, 426, 3211, doi: [10.1111/j.1365-2966.2012.21955.x](https://doi.org/10.1111/j.1365-2966.2012.21955.x)
- Liu, H. B. 2019, *ApJL*, 877, L22, doi: [10.3847/2041-8213/ab1f8e](https://doi.org/10.3847/2041-8213/ab1f8e)
- Long, F., Pinilla, P., Herczeg, G. J., et al. 2018, *The Astrophysical Journal*, 869, 17, doi: [10.3847/1538-4357/aae8e1](https://doi.org/10.3847/1538-4357/aae8e1)
- Longarini, C., Lodato, G., Rosotti, G., et al. 2025, *The Astrophysical Journal Letters*, 984, L17, doi: [10.3847/2041-8213/adc431](https://doi.org/10.3847/2041-8213/adc431)
- Loomis, R. A., Facchini, S., Benisty, M., et al. 2025, *exoALMA II: Data Calibration and Imaging Pipeline*. <https://arxiv.org/abs/2504.19870>
- Lovelace, R. V. E., & Hohlfeld, R. G. 1978, *ApJ*, 221, 51, doi: [10.1086/156004](https://doi.org/10.1086/156004)
- Lovelace, R. V. E., Li, H., Colgate, S. A., & Nelson, A. F. 1999, *ApJ*, 513, 805, doi: [10.1086/306900](https://doi.org/10.1086/306900)
- Lovelace, R. V. E., & Romanova, M. M. 2014, *Fluid Dynamics Research*, 46, 041401, doi: [10.1088/0169-5983/46/4/041401](https://doi.org/10.1088/0169-5983/46/4/041401)
- Lyra, W., Johansen, A., Klahr, H., & Piskunov, N. 2008, *Astronomy & Astrophysics*, 493, 1125, doi: [10.1051/0004-6361:200810797](https://doi.org/10.1051/0004-6361:200810797)
- Lyra, W., & Lin, M.-K. 2013, *The Astrophysical Journal*, 775, 17, doi: [10.1088/0004-637x/775/1/17](https://doi.org/10.1088/0004-637x/775/1/17)
- Ma, X., Huang, P., Yu, C., & Dong, R. 2025, *ApJ*, 979, 244, doi: [10.3847/1538-4357/ad9f2c](https://doi.org/10.3847/1538-4357/ad9f2c)
- Marino, S., Casassus, S., Perez, S., et al. 2015, *ApJ*, 813, 76, doi: [10.1088/0004-637X/813/1/76](https://doi.org/10.1088/0004-637X/813/1/76)
- Marino, S., Perez, S., & Casassus, S. 2015, *The Astrophysical Journal*, 798, L44, doi: [10.1088/2041-8205/798/2/L44](https://doi.org/10.1088/2041-8205/798/2/L44)
- Marr, M., & Dong, R. 2022, *ApJ*, 930, 80, doi: [10.3847/1538-4357/ac63ab](https://doi.org/10.3847/1538-4357/ac63ab)
- Meheut, H., Meliani, Z., Varniere, P., & Benz, W. 2012, *A&A*, 545, A134, doi: [10.1051/0004-6361/201219794](https://doi.org/10.1051/0004-6361/201219794)
- Mittal, T., & Chiang, E. 2015, *ApJL*, 798, L25, doi: [10.1088/2041-8205/798/1/L25](https://doi.org/10.1088/2041-8205/798/1/L25)
- Ono, T., Muto, T., Tomida, K., & Zhu, Z. 2018, *ApJ*, 864, 70, doi: [10.3847/1538-4357/aad54d](https://doi.org/10.3847/1538-4357/aad54d)
- Paardekooper, S.-J., Lesur, G., & Papaloizou, J. C. B. 2010, *The Astrophysical Journal*, 725, 146, doi: [10.1088/0004-637x/725/1/146](https://doi.org/10.1088/0004-637x/725/1/146)
- Pérez, S., Casassus, S., Baruteau, C., et al. 2019, *AJ*, 158, 15, doi: [10.3847/1538-3881/ab1f88](https://doi.org/10.3847/1538-3881/ab1f88)
- Quiroz, J., Wallack, N. L., Ren, B., et al. 2022, *The Astrophysical Journal Letters*, 924, L4, doi: [10.3847/2041-8213/ac3e62](https://doi.org/10.3847/2041-8213/ac3e62)

- Ragusa, E., Alexander, R., Calcino, J., Hirsh, K., & Price, D. J. 2020, MNRAS, 499, 3362, doi: [10.1093/mnras/staa2954](https://doi.org/10.1093/mnras/staa2954)
- Ragusa, E., Dipierro, G., Lodato, G., Laibe, G., & Price, D. J. 2017, MNRAS, 464, 1449, doi: [10.1093/mnras/stw2456](https://doi.org/10.1093/mnras/stw2456)
- Rau, U., & Cornwell, T. J. 2011, Astronomy & Astrophysics, 532, A71, doi: [10.1051/0004-6361/201117104](https://doi.org/10.1051/0004-6361/201117104)
- Regály, Z., Juhász, A., Sándor, Z., & Dullemond, C. P. 2012, MNRAS, 419, 1701, doi: [10.1111/j.1365-2966.2011.19834.x](https://doi.org/10.1111/j.1365-2966.2011.19834.x)
- Stadler, J., Benisty, M., Zagaria, F., et al. 2026, The Circumbinary Disk of HD 34700A: I. CO gas kinematics indicate spirals, infall, and vortex motions. <https://arxiv.org/abs/2601.15262>
- Stammler, S. M., Drżkowska, J., Birnstiel, T., et al. 2019, ApJL, 884, L5, doi: [10.3847/2041-8213/ab4423](https://doi.org/10.3847/2041-8213/ab4423)
- Stolker, T., Dominik, C., Avenhaus, H., et al. 2016, Astronomy & Astrophysics, 595, A113, doi: [10.1051/0004-6361/201528039](https://doi.org/10.1051/0004-6361/201528039)
- Tang, Y.-W., Guilloteau, S., Dutrey, A., et al. 2017, ApJ, 840, 32, doi: [10.3847/1538-4357/aa6af7](https://doi.org/10.3847/1538-4357/aa6af7)
- Tazzari, M., Beaujean, F., & Testi, L. 2018, MNRAS, 476, 4527, doi: [10.1093/mnras/sty409](https://doi.org/10.1093/mnras/sty409)
- Temmink, M., Booth, A. S., Leemker, M., et al. 2025, A&A, 693, A101, doi: [10.1051/0004-6361/202452175](https://doi.org/10.1051/0004-6361/202452175)
- Testi, L., Birnstiel, T., Ricci, L., et al. 2014, Dust Evolution in Protoplanetary Disks (University of Arizona Press), doi: [10.2458/azu_uapress_9780816531240-ch015](https://doi.org/10.2458/azu_uapress_9780816531240-ch015)
- Ueda, T., Kataoka, A., & Tsukagoshi, T. 2020, ApJ, 893, 125, doi: [10.3847/1538-4357/ab8223](https://doi.org/10.3847/1538-4357/ab8223)
- van der Marel, N., Cazzoletti, P., Pinilla, P., & Garufi, A. 2016, ApJ, 832, 178, doi: [10.3847/0004-637X/832/2/178](https://doi.org/10.3847/0004-637X/832/2/178)
- van der Marel, N., Pinilla, P., Tobin, J., et al. 2015, ApJL, 810, L7, doi: [10.1088/2041-8205/810/1/L7](https://doi.org/10.1088/2041-8205/810/1/L7)
- van der Marel, N., van Dishoeck, E. F., Bruderer, S., et al. 2013, Science, 340, 1199, doi: [10.1126/science.1236770](https://doi.org/10.1126/science.1236770)
- van der Marel, N., Birnstiel, T., Garufi, A., et al. 2021, AJ, 161, 33, doi: [10.3847/1538-3881/abc3ba](https://doi.org/10.3847/1538-3881/abc3ba)
- van der Plas, G., Menard, F., Canovas, H., et al. 2017, Astronomy & Astrophysics, 607, A55, doi: [10.1051/0004-6361/201731392](https://doi.org/10.1051/0004-6361/201731392)
- Vides, C. L., Sallum, S., Eisner, J., Skemer, A., & Murray-Clay, R. 2025, The Astrophysical Journal, 993, 178, doi: [10.3847/1538-4357/ae0932](https://doi.org/10.3847/1538-4357/ae0932)
- Wölfer, L., Barraza-Alfaro, M., Teague, R., et al. 2025, ApJL, 984, L22, doi: [10.3847/2041-8213/adc42c](https://doi.org/10.3847/2041-8213/adc42c)
- Yen, H.-W., & Gu, P.-G. 2020, ApJ, 905, 89, doi: [10.3847/1538-4357/abc55a](https://doi.org/10.3847/1538-4357/abc55a)
- Yoshida, T. C., Nomura, H., Tsukagoshi, T., et al. 2025, ApJ, 980, 50, doi: [10.3847/1538-4357/ad9f31](https://doi.org/10.3847/1538-4357/ad9f31)
- Zhu, Z., & Stone, J. M. 2014, ApJ, 795, 53, doi: [10.1088/0004-637X/795/1/53](https://doi.org/10.1088/0004-637X/795/1/53)
- Zhu, Z., Stone, J. M., Rafikov, R. R., & Bai, X.-n. 2014, ApJ, 785, 122, doi: [10.1088/0004-637X/785/2/122](https://doi.org/10.1088/0004-637X/785/2/122)
- Zhu, Z., Zhang, S., Jiang, Y.-F., et al. 2019, ApJL, 877, L18, doi: [10.3847/2041-8213/ab1f8c](https://doi.org/10.3847/2041-8213/ab1f8c)